TISSUE ENGINEERING: Part A
Volume 25, Numbers 7 and 8, 2019

DOI: 10.1089/ten.tea.2018.0155

termis
Tissue Engineering
& Regenerative Medicine
International Society

ORIGINAL ARTICLE

Size-Dependent Cortical Compaction Induces Metabolic Adaptation in Mesenchymal Stem Cell Aggregates

Brent M. Bijonowski, MSc,[1] Susan I. Daraiseh, PhD,[2] Xuegang Yuan, MSc,[1] and Teng Ma, PhD[1]

Spontaneous assembly of human mesenchymal stem cells (hMSCs) into three-dimensional aggregates enhances stem cell properties and enables formation of heterotypic organoids, which has significant implication in cell therapy and tissue engineering. Although metabolic reprograming toward glycolysis is a salient feature of multicellular aggregates and it has commonly been attributed to oxygen diffusion limitations, recent studies have instead observed a limited decline in oxygen tension, in hMSC aggregates, challenging this view. Although aggregation of a dispersed cell population involves changes in both the physical and molecular environment, most studies to date have focused on molecular gradients with limited investigation in biomechanical stress on the fate of aggregated cells. The objective of this study is to investigate how the mechanical gradient arising from aggregation-induced cortical compaction alters the metabolic profile of human adipose-derived mesenchymal stem cells by testing the hypothesis that size-dependent compaction in aggregates leads to differential cortical stress, which induces metabolic reprogramming. Herein, we show that aggregation of multiple sizes covering a wide range of interest does not lead to hypoxic core formation but instead varying levels of cortical compaction, indicated by the balance between stress fiber formation and the deposition of extracellular matrix proteins, resulting in corresponding levels of metabolic reconfiguration. Increased glycolytic metabolism, increased mitochondrial fission, and increased release of aldolase A were all observed as a result of cortical compaction. Chemical inhibition with Gleevec, Wortmannin, and Y27632 almost completely abolishes the cortical stress-induced enhancement in glycolytic properties. Our findings demonstrate that aggregation-induced biomechanical stress plays a central role in driving metabolic reprogramming.

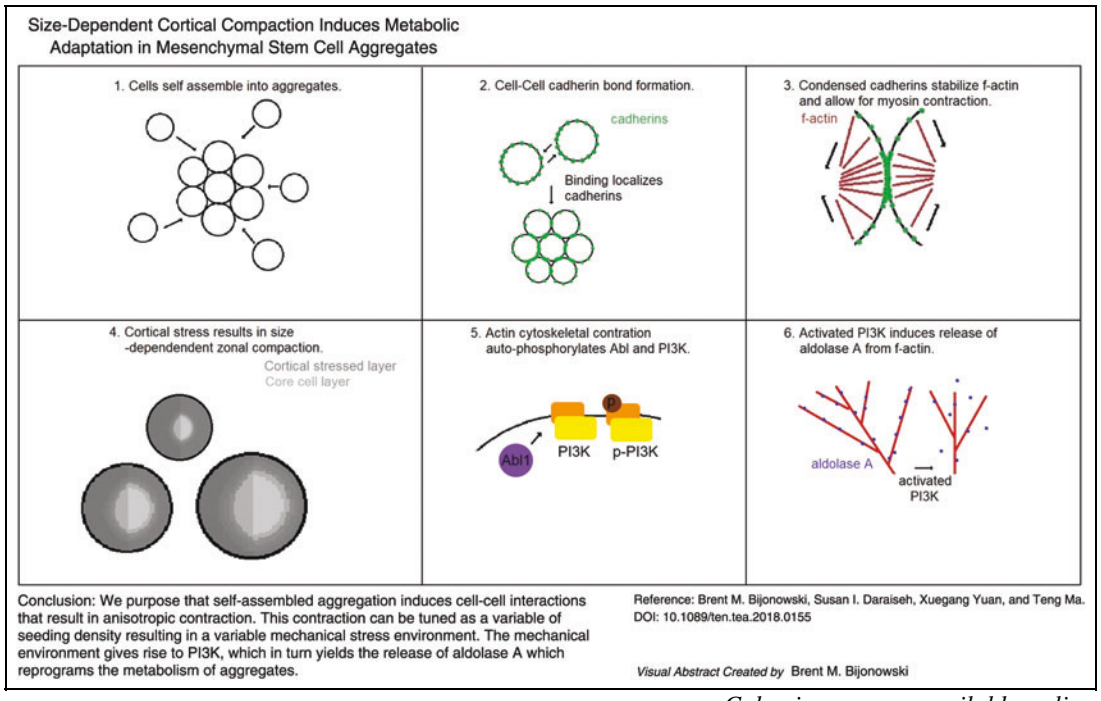

Color images are available online.

Keywords: aggregation, metabolic reprogramming, adipose-derived stem cells, oxygen tension, PI3K, aldolase A

Impact Statement

This study reveals that multicellular aggregation induces metabolic reprogramming via mechanical compaction in lieu of formation of a hypoxic core. Utilizing biomechanical knowledge gained from planar culture, we set forth a novel three-dimensional (3D) model of size-dependent cortical compaction and demonstrated its role in metabolic reconfiguration. Ultimately, this study establishes mechanical compaction and its spatial gradients as key regulatory factors and design parameters in the development of 3D human adipose-derived mesenchymal stem cell aggregates.

[1]Dept. of Chemical and Biomedical Engineering, FAMU-FSU College of Engineering, Florida State University, Tallahassee, Florida.
[2]Dept. of Biomedical Sciences, College of Medicine, Florida State University, Tallahassee, Florida.

Introduction

Human mesenchymal stem cells (hMSCs) from bone marrow (BM-hMSC) or adipose tissue (hASC) have gained widespread use in cell therapy and tissue regeneration. Although traditionally expanded and delivered as dispersed cells, an increasing number of studies have shown that aggregation enhances hMSC functional properties such as the secretion of anti-inflammatory cytokines,[1,2] survival in an ischemic environment post-transplantation, and enhanced tissue repair in various injuries.[3–6] In addition, hMSC-driven condensation enables self-assembly of dispersed and heterotypic cell populations into vascularized and complex organ buds, demonstrating hMSCs' innate ability as mesenchymal cells to aid the assembly of functional tissues or organoids via cell-mediated organization.[7] To exploit hMSCs' unique functional properties in three-dimensional (3D) organization, it is fundamental to understand the mechanism underpinning hMSC properties in 3D aggregates.

Self-assembly of a dispersed cell population into aggregates involves drastic changes in cell morphology, cell–cell interaction, and changes to the molecular niche, culminating in a heterogeneous cellular organization that is characterized by both molecular and biomechanical gradients.[8,9] Increased restriction to oxygen, due to increased diffusion distance and an immutable zero-order oxygen consumption rate (OCR),[9,10] has been attributed as the major factor in the generation of a hypoxic/necrotic core, which alters cellular properties.[8,9] However, recent literature has shown minimal reduction of oxygen tension in hMSC aggregates,[10] and another recent study has shown that encapsulation of MSCs as single cells in a polymer gel, thereby increasing the diffusion barrier, has limited impact on hMSC secretory profile. By contrast, hMSC aggregates with and without polymer encapsulation have enhanced secretory profiles; suggesting that cell–cell aggregation rather than a diffusion barrier is required for hMSC functional enhancement.[11,12]

Elasticity plays a significant role in regulating hMSC fate and gene expression profiles,[13] which hMSCs can sense via cellular contraction.[14] Aggregation induces a lower cellular elastic niche than planar culture, and when hMSCs were cultured on plates matching the modulus of aggregates they showed similar upregulation of select proteins, and the induction of some pro- and anti-inflammatory genes, though to a lesser extent than after aggregation, suggesting the importance of cell–cell contact in conjunction with surface elasticity.[13] Compared with diffusion-induced molecular gradients, little is known about the role of biomechanical forces, and the characteristics of their associated gradients in 3D aggregates in regulating hMSC properties. Aggregated hMSCs display a heterogenous morphology with a cortical region of flattened cells and a more regular and rounded morphology in the core.[15,16] To date, the effects of biomechanical cues on hMSC fate have been primarily studied in planar culture by varying mechanical properties, but these results provide limited insight because of the limited cell–cell interactions found in planar culture.

This article sets out to test the hypothesis that size-dependent compaction in hASC aggregates leads to differential cortical stress, which induces metabolic reprogramming independent of an oxygen gradient. We show that hASC aggregates have limited reduction of oxygen tension but exhibit size-dependent cortical compaction, which leads to PI3K activation, increased release of aldolase A (AldoA), and, ultimately, metabolic reprogramming. These results provide a novel connection between actomyosin-mediated cortical compaction and the restoration of a primitive glycolytic phenotype in hASC aggregates and they have a significant implication in the clinical application of hASC aggregates.

Materials and Methods

Culture of hASCs

Frozen hASCs at passage 1 were obtained from the Tulane Center for Stem Cell Research and Regenerative Medicine. The hASCs were isolated from the liposate of healthy donors and were expanded in minimum essential medium-alpha (αMEM) (Life Technologies, Carlsbad, CA) supplemented with 1% penicillin/streptomycin (Life Technologies) and 10% fetal bovine serum (Atlanta Biologicals, Lawrenceville, GA) to form complete culture media (CCM) on 150-mm tissue culture Petri dishes (Corning, Corning, NY) in a standard 5% CO_2 incubator. When 80–90% confluence was reached, cells were trypsinized and subcultured. The culture media were changed every 3 days. To generalize hASC variability, three different donors were pooled and used in the experiments from passage 5 to 7.[17–19] Aggregates from single donors were also analyzed but did not show significant difference to those of the pooled donors (data not shown). All culture reagents were purchased from Sigma Aldrich (St. Louis, MO) unless otherwise noted.

Aggregate formation and treatment with PI3K/Akt modulators

Once cells reached 90% confluence, they were trypsinized and pelleted. The pellet was resuspended in CCM to a final concentration of 250,000 cells/mL. Either 200, 120, or 40 μL was seeded into the well of an ultra-low attachment (ULA) 96-well plate. The aggregates were allowed to homogenize over 72 h, with media changes every 24 h. A single aggregate was observed per well. The aggregates were tracked individually, and the morphologies were imaged with an Olympus IX70 microscope (Center Valley, PA).

To examine the effect of PI3K on spheroid culture, the CCM was conditioned with SF1670 or Wortmannin (Enzo, Farmingdale, NY) at final concentrations of 4 and 40 μM, respectively. After an additional 24 h in the incubator, the aggregates were tested.

In addition, to test the compaction pathway signaling, Y27632 dichloride and Gleevec (Imatinib Mesylate) (Biogems, Westlake Village, CA) were used at 20 μM.

Analysis of aggregate size and DNA content

Aggregates were visualized by using an Olympus IX70 microscope, and the physical properties were determined by using ImageJ. The volumes of the individual aggregates were calculated from an ellipsoid approximation by using observed major and minor axes, whereas the DNA content of the individual aggregate was used to calculate the number of cells. Briefly, single hASC aggregates were washed in phosphate-buffered saline (PBS) and digested in proteinase K overnight. Samples and standards were then aliquoted in triplicate. PicoGreen (Life Technologies) was added, and

the plate was then read in a SpectraMax M5 plate reader (Molecular Devices, Sunnyvale, CA). The cell number in each aggregate was determined by dividing the PicoGreen quantity by 9.3 pg/cell.[20]

Oxygen, glucose, and lactate concentration and consumption rates

After 24 h in culture, the media were replaced with CCM containing 50 μM tris(bipyridine)ruthenium(II) chloride (Ru-dpp). Ru-dpp is a fluorescent organometallic compound that fluoresces in the absence of oxygen and is quenched in the presence of sufficient oxygen.[21] Baseline oxygen concentration was determined as CCM with Ru-dpp but without cells. In addition, a negative control was taken as CCM without cells and Ru-dpp. The culture was placed in a 5% CO_2 incubator for 3 h; the spheroids were then washed in PBS, and imaged on a Cytation 5 Imaging Platform (Biotek, Winooski, VT) with thermal and gas control. Fluorescent excitation occurred at 450 nm, and emission was measured at 635 nm. Images were recorded, and they were processed by using a custom Matlab (Mathworks, Natick, MA) program (Supplementary Data). Briefly, fluorescent images were converted to intensity maps, and using a standard curve they were converted to O_2 concentration profiles. A linearized steady-state Fickian diffusion model with zero-order consumption was used to calculate the OCR with the assumption that a hypoxic core was not present. A zero-order model was used instead of a Michaelis-Menten; since the OCR did not vary significantly over the range of interest, a zero-order approximation was sufficient. The surface of the aggregate was assumed to be at equilibrium with the saturated solution. This was validated by the limited volume and depth such that diffusion was sufficient. Thiele modulus was calculated by using the mathematical model give in van Winkle *et al.* $\phi^2 = \frac{OCR\rho\left(\frac{d}{4}\right)^2}{C_{Bulk}D_{O_2}}$ where φ^2 is the Thiele modulus, d is the diameter of the aggregate, ρ is the packing density of the aggregate in cells/unit volume, C_{Bulk} is the concentration of oxygen in the surrounding liquid, and D_{O2} is the diffusion rate of oxygen through the aggregate (water).[9]

Conditioned media from culture were pooled from each condition at 96 h. Media were spun down and analyzed on a YSI 2500 Biochemistry Analyzer (Yellow Springs, OH) for lactate and dextrose.

Mitochondrial activity

Spheroids were washed with PBS and resuspended in media containing 6 μM resazurin, a nonfluorescent compound that is converted to resorufin by the mitochondrion. Resorufin is fluorescent and was measured on a SpectraMax M5 plate reader (Molecular Devices) with excitation at 570 and emission at 585. The concentration of resorufin was measured in a kinetic fashion, and the rate of turnover of resazurin was calculated.

Intracellular and glycolytic ATP

Spheroids were washed with PBS and resuspended in PBS. The spheroids were then boiled for 15 min before being spun down at top speed for 15 min. The supernatant was collected, and a 10-μL sample was used. The concentration of ATP was determined with a Luciferase-Luciferin solution that luminesces in response to ATP (Molecular Probes, Eugene, OR). Glycolytic ATP was determined by adding 2-deoxy-D-glucose (2DG) (5 mM) in CCM to the spheroids for 12 h before sampling[22]; 2DG blocks glycolysis, and the percentage of glycolytic ATP was defined as the difference between non-2DG treated and 2DG treated divided by non-2DG.

AldoA activity

A Boyer's modification of the hydrazine assay[23] was carried out on total cell lysate and permeabilized spheroid cells to measure AldoA activity. Spheroids at day 4 were washed in PBS, and then half were suspended in 0.5% Tween 20 for 30 min to permeabilize them. The other half were lysed in RIPA buffer. A solution of Fructose-1,6-bisphosphate(Fruc-16PB) and hydrazine sulfate was mixed, and absorbance was measured every minute for 10 min at 240 nm as a control. Next, samples of lysate or permeabilized cells were added to the solution and the absorbance was read for an additional 10 min at 240 nm. Readings were made on a SpectraMax M5.

Mitochondrial imaging

For mitochondria imaging, cells were incubated with 100 nM MitoTracker Red CMXRos (Molecular Probe) in CCM at 37°C for 30 min. After washing, the cells were then incubated with 3.7% formaldehyde at 20°C for 15 min. Imaging was performed by using an Olympus IX70 microscope. Mitochondrial-shape factors, including circularity ([4 × π × area]/perimeter^2) and aspect ratio (largest diameter/smallest diameter), were quantified by using ImageJ (NIH software).

Western blot and immunocytochemistry staining

Aggregates and planar cells were washed with PBS, lysed in RIPA buffer (150 mM sodium chloride, 1.0% Trition X-100, 0.5% sodium deoxycholate, 0.1% sodium dodecyl sulfate, 50 mM Tris, pH 8, 2 μg/mL Aprotinin, 5 μg/mL Leupeptin, 5 μg/mL Antipain, 1 mM PMSF), and homogenized by sonification using a Sonic Dismebrator 100 (Fisher Scientific, Hampton, NJ). Samples were then digested for 20 min on ice, and they were spun down at 14,000 rpm for 20 min. The supernatant was collected, and a Bradford assay was carried out to determine the protein concentration. The samples were denatured at 95°C in 2 × Laemmli Sample buffer. Proteins were separated by 10% BIS-Tris-SDS gels and transferred onto a nitrocellulose membrane (Bio-Rad, Hercules, CA). For the detection of nonphosphorylated proteins, the membranes were blocked for 30 min in 3% skim milk (w/v) in Tris-buffered saline with tween 20 (TBST) (10 mM Tris-HCl, pH 7.5, 150 mM NaCl, and 0.1% Tween 20 [v/v]). To detect phosphorylated proteins, blocking was carried out in 3% BSA (w/v), in TBST. Membranes were incubated overnight in the presence of the primary antibody diluted in the corresponding blocking buffer at 4°C. Primary antibodies α-tubulin and β-actin are purchased from Santa Cruz Biotechnology (Dallas, TX); collagen I, fibronectin, and p-vinculin-Y822 from Abcam (Cambridge, MA); and vinculin, p-vinuclin-Y1065, and p-PI3K from Invitrogen (Waltham, MA). All other antibodies

were purchased from Cell Signaling (Danvers, MA). Afterward, the membranes were washed four times for 10 min each with TBST and then incubated with an IR secondary (LI-COR, Lincoln, NE) at 1:10,000 for 90 min at room temperature. Blots were washed four times for 10 min each with TBST and processed by using the LI-COR Odyssey. Images were analyzed in ImageJ.

Polymerase chain reaction

Aggregate or planar culture pellets were homogenized with a Sonic Dismebrator 100 (Fisher Scientific), and total RNA was extracted by using an RNeasy Mini Kit (Qiagen, Valencia, CA). Two micrograms of total RNA was used to carry out reverse transcription, with anchored oligo-dT primers (Operon, Louisville, KY) and Superscript III (Invitrogen, Grand Island, NY). Specific primers for target genes were designed in the software Oligo Explorer 1.2 (Genelink, Hawthorne, NY). Beta-tubulin was used as an endogenous control for normalization. Real-time reverse transcriptase-polymerase chain reaction (RT-PCR) reactions were performed on an ABI7500 instrument (Applied Biosystems, Foster City, CA), using SYBR Green PCR Master Mix. After amplification, the quality and primer specificity were verified. Variation in gene expression was evaluated by using the comparative Ct method: $2^{-(\mathrm{CtTreatment} - \mathrm{CtControl})}$, based on the expression of the target gene (normalized to beta-tubulin).

Statistics

A one-tailed Student's *t* test was used to compare two groups, and for multiple-group comparison a one-way analysis of variance with Tukey's *post hoc* analysis was performed by using a statistical software (SPSS, Chicago, IL; www.spss.com). All data are presented as a mean value with its standard deviation indicated (mean ± SD). Differences were considered to be statistically significant when the *p* values were <0.05.

Results

Aggregation results in limited reduction in oxygen tension by reprograming energy metabolism toward glycolysis

ASCs self-assembled rapidly in ULA plates to form spherical cell–cell aggregates. Ru-dpp staining was carried out to analyze the oxygen profile throughout the aggregates. Utilizing a custom Matlab program (Supplementary Data), the Ru-dpp images (Fig. 1A) were converted to oxygen concentration maps (Fig. 1B). From these, it was determined that the oxygen tension differed by ~3% in the 10k spheroids and ~11% in the 50k spheroids from bulk oxygen dissolved in CCM. Ru-dpp oxygen profiles were applied to a Fickian diffusion model to determine the effect of aggregation on OCR, which showed a significant increase between 10k and 50k, 38 ± 1.7 and 48 ± 1.5 fmol/cell/h, respectively (Fig. 1C).

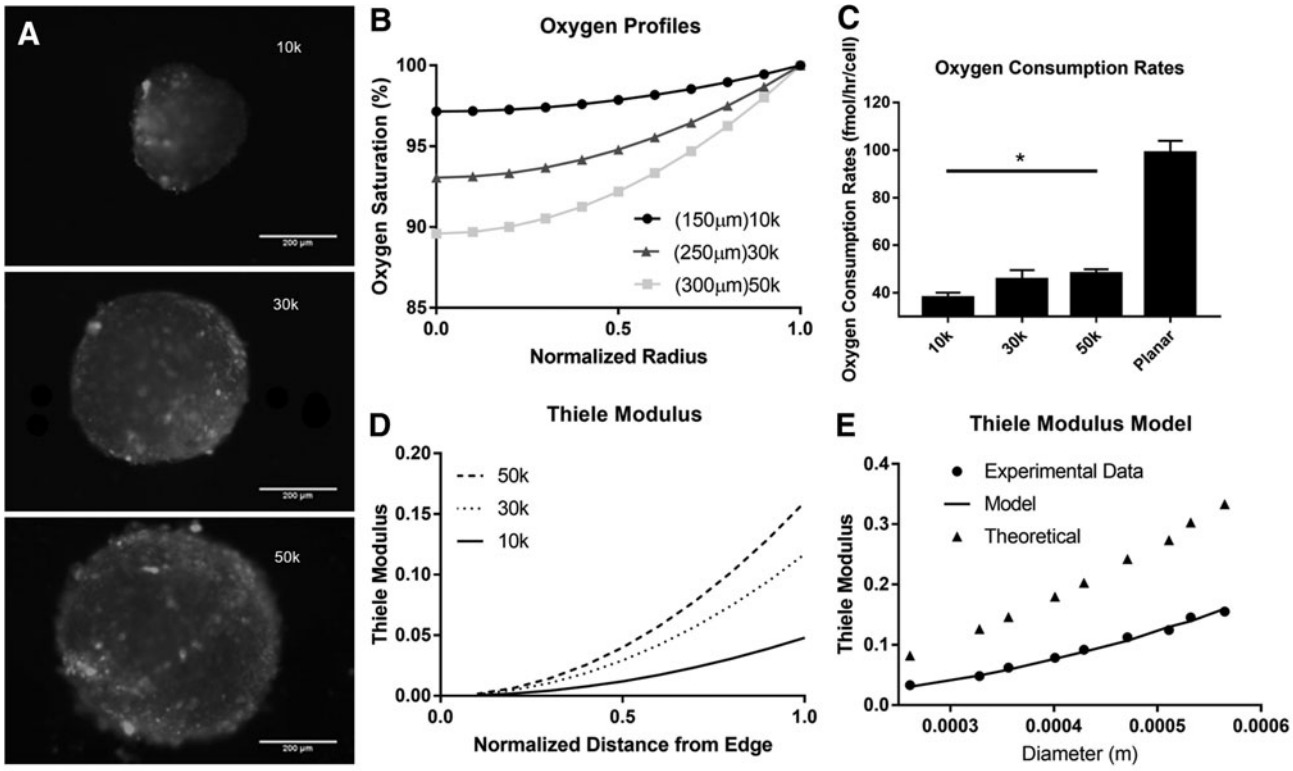

FIG. 1. Biomolecular gradient and diffusion in hASC. **(A)** Ru-dpp images of oxygen concentration in 10k, 30k, and 50k aggregates (scale bar is 200 μm). **(B)** Normalized radial oxygen profiles for size-dependent aggregates (represents average for size). **(C)** Oxygen consumption rates for planar, aggregate sizes. **(D, E)** Normalized radial and edge Thiele modulus for aggregates. Edge modulus model: $\phi^2 = \frac{\left(\frac{v_{max}[O_2]}{K_m+[O_2]}+\frac{\alpha}{\rho}+\beta\right)\left(\frac{d}{4}\right)^2}{C_{Bulk}D_{O_2}}$ ($v_{max} = 1.0\text{E-}13$ mol/cell/h, $K_m = 2\text{E-}7$ mol/m^3, $\alpha = 21.54$ mol/m^3/h, $\beta = -1.34\text{E-}13$ mol/cell/h) Data represent the mean of at least three independent determinations; errors represent the standard error in the mean. *$p < 0.05$. hASCs, human adipose-derived stem cells.

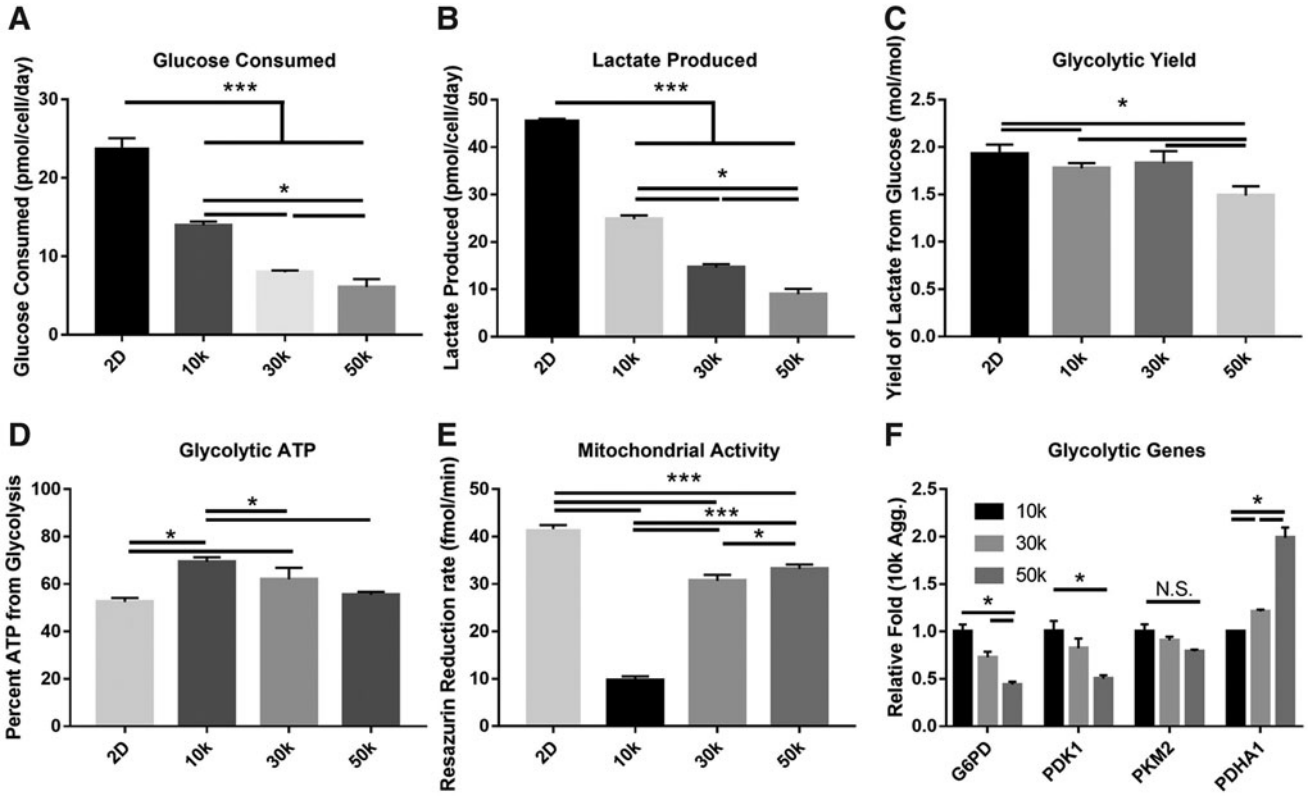

FIG. 2. Aggregation-induced reprogramming of metabolic profiles. **(A–C)** Plots of glucose consumed and lactate produce showing the level of metabolic reprogramming, along with the yield ratios. **(D)** Percentage of ATP as a result of aggregation. **(E)** Percentage of oxidative phosphorylation as determined by mitochondrial activity. **(F)** qPCR results for glycolytic genes. Data represent the mean of at least three independent determinations; errors represent the standard error in the mean. $^*p < 0.05$. ATP, adenosine triphosphate; qPCR, quantitative polymerase chain reaction.

Differences in the OCR lead to examining the Thiele modulus, which was calculated by using the equation described in van Winkle *et al.*[9] The Thiele modulus failed to predict the experimental data when fitted with measured packing density and the OCR from planar culture. Instead, an OCR model was derived that utilizes a modified Michaelis-Menten equation and takes into account biomechanical compaction $v = \frac{v_{max}[O_2]}{K_m + [O_2]} + \frac{\alpha}{\rho} + \beta$ Here, the Michaelis-Menten kinetic parameters have been modified to include alpha divided by the packing density plus a correction constant. This correction to the OCR nearly perfectly predicts the experimental Thiele Modulus data points (Fig. 1E).

Glycolytic reprogramming in the aggregate was further assessed by analyzing the glucose/lactate levels, ATP from glycolysis, and the mitochondrial activity. Both glucose consumption (Fig. 2A) and lactate production (Fig. 2B) were significantly reduced by aggregation decreasing from 23.8 ± 1.0 and 45.8 ± 0.1 pmol/cell/day in planar to 14.0 ± 0.4 and 24.8 ± 0.7 pmol/cell/day in 10k. Aggregation also induced a significant inverse size-dependent trend among the aggregates. Both glucose consumption and lactate production were significantly decreased to 6.83 ± 0.93 and 8.98 ± 0.1 pmol/cell/day in the 50k spheroids (Fig. 2A, B). Similarly, the yield of lactate from glucose showed a significant reduction as size increased (Fig. 2C), and glycolytic ATP significantly increased as a result of aggregation from $52.1\% \pm 1.6\%$ in planar to 70.8 ± 1.9 in 10k; however, glycolytic ATP dropped off as size increased, falling to $50.1\% \pm 1.3\%$ in the 50k aggregate (Fig. 2D). Analysis of metabolic profile was followed up by analyzing the effect of aggregation on mitochondrial function. Mitochondrial activity exhibited significantly higher activity in planar culture than in aggregates; there was also a significant size-dependent increase in resazurin reduction rate, ranging from 9.69 ± 0.73 fmol/min in 10k to 33.2 ± 0.76 in 50k (Fig. 2E). To assess whether the effects were purely volume reduction, key metabolic genes were analyzed by qualitative polymerase chain reaction (qPCR). Glucose-6-phosphate dehydrogenase (*G6PD*) and pyruvate dehydrogenase kinase 1, both of which are essential to handling glucose anaerobically, were significantly higher in the 10k aggregates than in the 50k aggregates. The glycolytic enzyme pyruvate kinase isozyme M2 (*PKM2*) also showed an increase in 10k over 50k but was nonsignificant. The 50k aggregate, however, showed significantly higher levels of the mitochondrial pyruvate dehydrogenase alpha 1 (*PDHA1*) (Fig. 2F).

Aggregation induces size-dependent cortical compaction and zonal distribution of stress fibers

Cellular reprogramming, including metabolic, owing to biomechanical cues has been analyzed in planar culture extensively, and these results have shown the importance of the mechanotransduction pathway and cell–cell/extracellular matrix (ECM) interactions to reprogramming.[24–26] Due to the practical limitations of modeling the stress of individual cells,[27] it is necessary to relay on imaging as a surrogate for

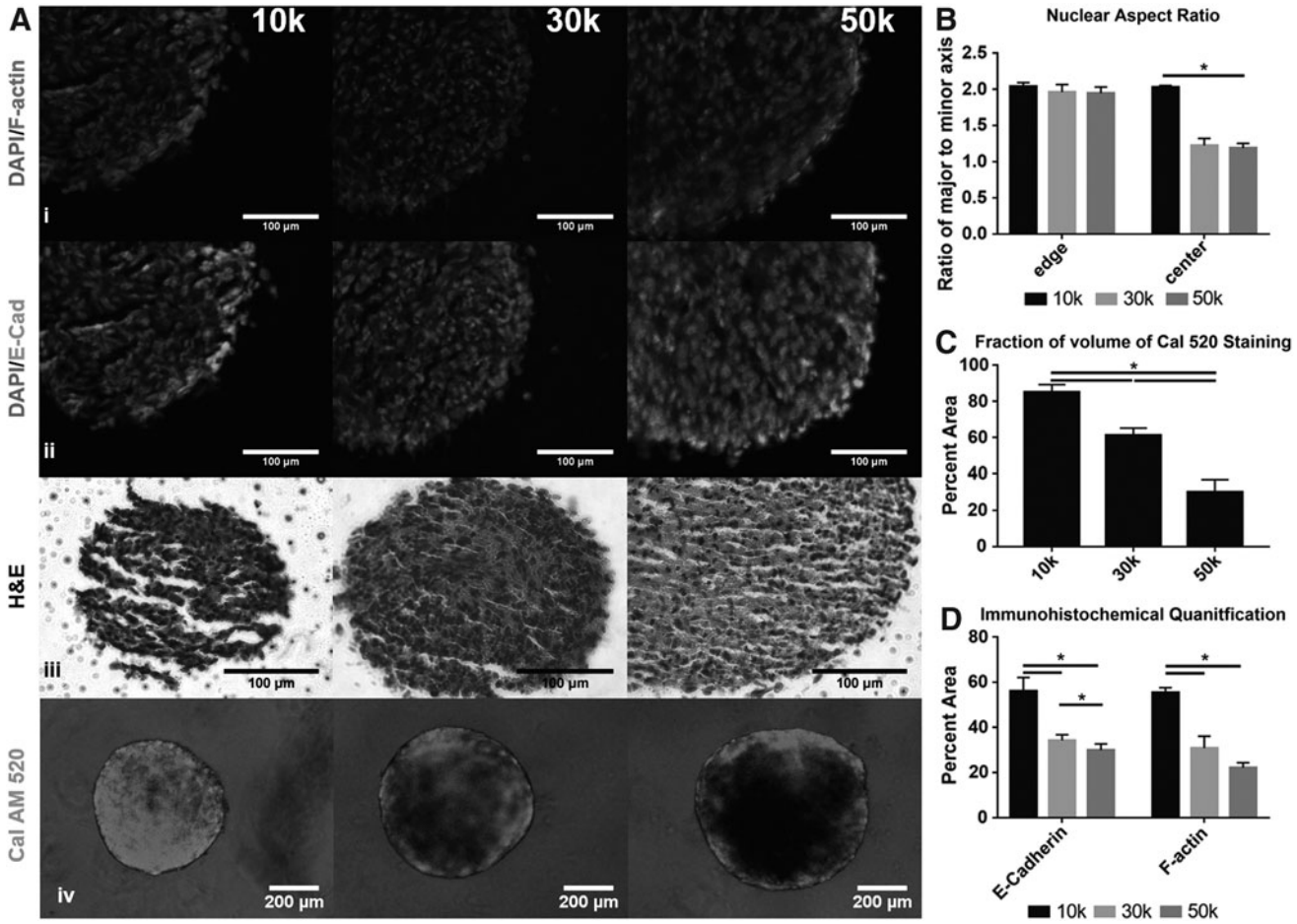

FIG. 3. ASC aggregates show a size-dependent compaction. **(A) (i)** Immunohistochemical staining for nuclei and F-actin. **(ii)** Immunohistochemical staining for E-cadherin. **(iii)** Hematoxylin and eosin images for 10k, 30k, and 50k (scale bar is 100 μm). **(iv)** Cal AM 520 staining on whole ASC aggregates (scale bar is 200 μm) **(B)** Nuclear compaction as determined by observation of DAPI-stained nuclear aspect ratio. **(C)** Volume fraction of CalAM 520 stained aggregates as calculated by imaged radius. **(D)** Volume fraction of F-actin and E-cadherin as calculated by imaged radius. Data represent the mean of at least three independent determinations; errors represent the standard error in the mean. ASCs, adipose-derived mesenchymal stem cells.

determining the stress environment. Immunohistochemical staining for fibrous actin (F-actin), the major component of stress fibers, and DAPI (Fig. 3Ai; Supplementary Fig. S1) showed a distinct cortical F-actin and nuclear condensation ring around all the aggregates (Fig. 3B, D); however, the cortical ring reduced with increasing aggregate size.

Due to the nature of multicellular aggregation inducing cell–cell interactions, the adhesion molecule E-cadherin and its downstream mechanotransductive pathway were analyzed. Previous literature has shown that mechanical stress induced in MSCs by pulling with magnetic beads labeled with E-cadherin leads to Abl1 activation and the subsequent phosphorylation of α-catenin and vinculin at Y822.[28] The expression of E-cadherin mirrored F-actin showing intense cortical regions but reducing with increasing size (Fig. 3Aii, D). Similarly, protein expression levels of E-cadherin, α-catenin, and p-Y822 vinculin were all increased in the smaller aggregate but decreased with increasing size (Fig. 4A). Due to the trend of decreasing E-cadherin interaction with increasing size, the cell–ECM interaction was explored as a possible alternative, and analysis of the core regions by hematoxylin and eosin showed more extensive collagen deposition in the 30k and 50k (Fig. 3Aiii). Similarly, gene expression of collagen 1, fibronectin, and focal adhesion kinase (FAK) all showed increased prevalence in the larger aggregates, which was reflected by Western blot analysis as well. Western blot also showed a higher degree of p-FAK and p-vinculin (Y1065), both of which are signs of cell–ECM stress (Fig. 4).

Actomyosin contraction is dependent on the presence of Ca^{2+} to bind calmodulin and activate myosin light chain, the myosin motor, and to further bind to troponin C, allowing for myosin binding to actin. Ca^{2+} was visualized by staining with Cal 520AM and showed significantly thicker cortical intensity in the 10k, accounting for 85% ± 3% of the total volume while only accounting for 30% ± 5% in the 50k (Fig. 3Aiv, C).

Cortical stress activates PI3K altering metabolism and mitochondrial activity

To determine the level of mechanotransduction signaling carried out by PI3K, it was perturbed via addition of

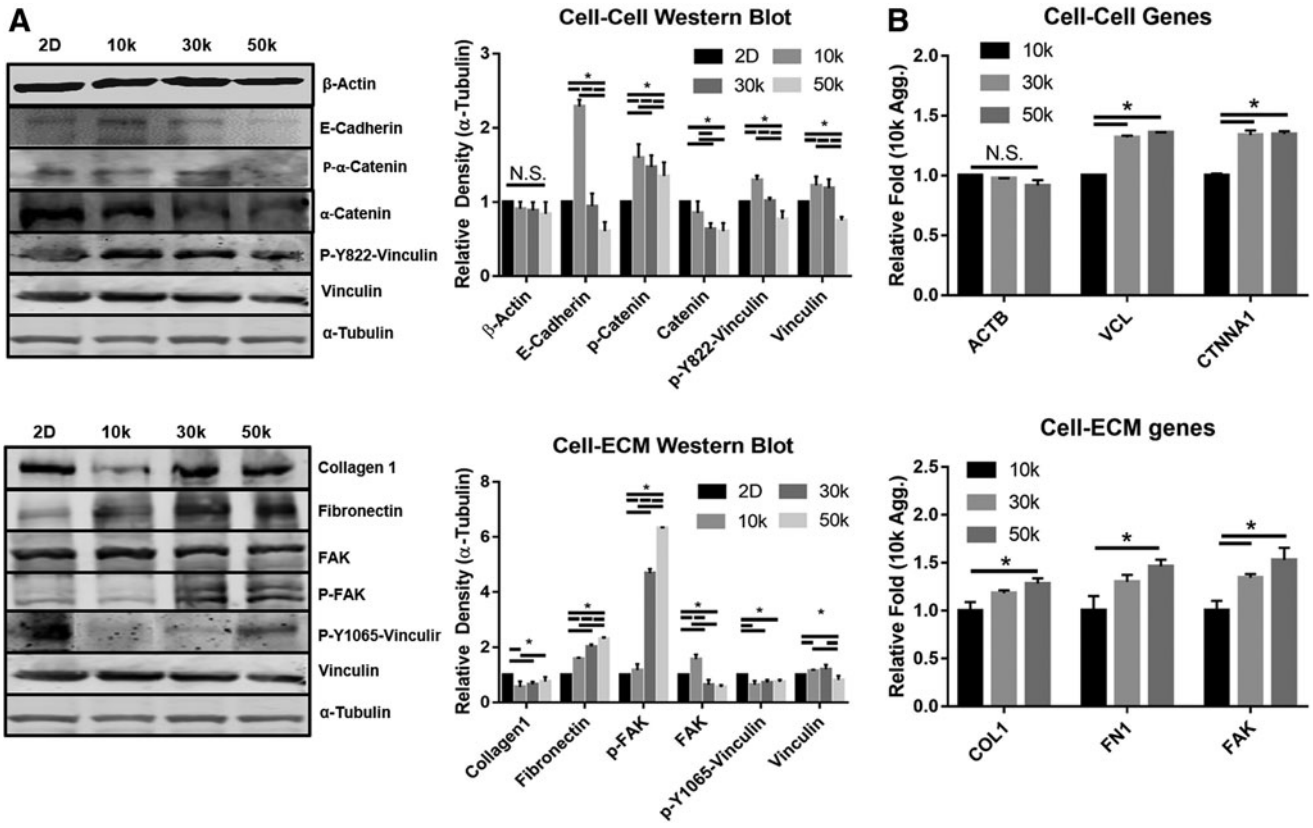

FIG. 4. Western blot analysis for mechanical signal transduction. **(A)** Blots and density reading for aggregation-induced and size-dependent mechanical phosphorylation with standardized tubulin. **(B)** qPCR results for cell–cell and cell–ECM proteins. Data represent the mean of at least three independent determinations; errors represent the standard error in the mean. ECM, extracellular matrix.

SF1670, a PTEN inhibitor that stabilizes p-PI3K, and Wortmannin, a general p-PI3K/Akt inhibitor.[29,30] When using SF1670, we observed a nonsignificant decrease in the OCR for the 10k, 30k, and 50k. Wortmannin, however, significantly increased OCR for 10k, 30k, and 50k (Table 1). To analyze the effect of compaction-mediated PI3K on OCR, we treated the aggregates with Y27632, which inhibits ROCK, leading to significantly increased OCR for all sizes (Table 1). Previously, we had shown that treatment with Y27632 increased the diameter of the aggregate and significantly reduced the

TABLE 1. VALUES ILLUSTRATING THE EFFECT OF SF1670 AND WORTMANNIN TO ALTER PI3K PHOSPHORYLATION LEVEL AND ITS EFFECT ON: OXYGEN UPTAKE RATES FOR 10K, 30K, AND 50K WITH AND WITHOUT CHEMICAL TREATMENT, MITOCHONDRIAL ACTIVITY AS A RESULT OF AGGREGATION AND CHEMICAL TREATMENT, AND SHIFT TO GLYCOLYSIS

Aggregate size	*Treatment*	*OCR (fmol/h/cell)*		*Mitochondrial activity (fmol/min/cell)*		*Percent glycolytic ATP*	
		Mean	*Significance*	*Mean*	*Significance*	*Mean*	*Significance*
10k	a-Control	38.0 ± 1.7	c,d	10.4 ± 0.4	b,c,d	69.2 ± 2.0	b,c,d
	b-SF1670	35.1 ± 9.6	c,d	3.7 ± 0.0	a,c,d	72.1 ± 1.4	a,c,d
	c-Wortmannin	52.0 ± 0.8	a,b,d	18.7 ± 0.4	a,b,d	43.7 ± 1.6	a,b
	d-Y27632	55.6 ± 0.9	a,b,c	23.4 ± 0.8	a,b,c	46.0 ± 4.2	a,b
30k	a-Control	45.7 ± 3.2	c,d	29.7 ± 0.7	b,c,d	62.0 ± 4.7	b,c,d
	b-SF1670	44.8 ± 11.3	—	5.1 ± 0.5	a,c,d	73.8 ± 3.6	a,c,d
	c-Wortmannin	58.8 ± 2.4	a	37.7 ± 1.0	a,b	48.6 ± 2.9	a,b
	d-Y27632	61.0 ± 1.6	a	39.7 ± 1.2	a,b	44.6 ± 2.7	a,b
50k	a-Control	48.0 ± 1.5	c,d	32.4 ± 0.0	b,c,d	55.4 ± 1.5	b,c,d
	b-SF1670	44.8 ± 3.4	c,d	6.1 ± 0.7	a,c,d	66.4 ± 5.6	a,c,d
	c-Wortmannin	58.6 ± 1.4	a,b	56.3 ± 5.8	a,b	44.1 ± 2.1	a,b
	d-Y27632	62.7 ± 1.7	a,b	57.2 ± 2	a,b	48.7 ± 1.3	a,b

Significance connects the given row to the appropriate lettered row: (a) untreated control, (b) SF1670 treated, (c) Wortmannin treated, and (d) Y27632 treated. Data represent the mean of at least three independent determinations; errors represent the standard error in the mean.
ATP, adenosine triphosphate; OCR, oxygen consumption rate.

Table 2. Individual Aggregation-Induced Reprogramming Values for: Glucose Consumption and Lactate Production Rates, Yield of Lactate from Glucose

		Glucose consumed (pmol/cell/day)		*Lactate produced (pmol/cell/day)*		*Glycolytic yield (mol/mol)*	
Aggregate size	*Treatment*	*Mean*	*Significance*	*Mean*	*Significance*	*Mean*	*Significance*
10k	a-Control	14.0 ± 0.4	c,d	24.8 ± 0.7	b,c,d	1.8 ± 0.0	b,c
	b-SF1670	15.6 ± 0.3	a,c,d	19.2 ± 0.5	a,c,d	1.2 ± 0.0	a,c,d
	c-Wortmannin	7.4 ± 0.3	a,b	6.2 ± 0.3	a,b,d	0.8 ± 0.1	a,b,d
	d-Y27632	6.2 ± 0.7	a,b	9.2 ± 0.8	a,b,c	1.5 ± 0.3	b,c
30k	a-Control	8.0 ± 0.2	b,c,d	14.6 ± 0.6	b,c,d	2.0 ± 0.0	b,c,d
	b-SF1670	12.2 ± 0.0	a,c,d	17.3 ± 0.1	a,c,d	1.4 ± 0.0	a,c
	c-Wortmannin	6.0 ± 0.2	a,b,d	4.5 ± 0.0	a,b,d	0.7 ± 0.0	a,d
	d-Y27632	4.3 ± 0.2	a,b,c	6.3 ± 0.4	a,b,c	1.5 ± 0.1	a,b,c
50k	a-Control	6.1 ± 0.9	b,d	9.0 ± 1.0	b,c,d	1.9 ± 0.1	b,c
	b-SF1670	11.3 ± 0.1	c,d	16.7 ± 0.0	a,c,d	1.5 ± 0.0	a,c
	c-Wortmannin	4.5 ± 0.2	a,b,d	3.2 ± 0.1	a,b	0.7 ± 0.0	a,b,d
	d-Y27632	2.2 ± 0.1	a,b,c	3.1 ± 0.2	a,b	1.4 ± 0.2	c

Significance connects the given row to the appropriate lettered row: (a) untreated control, (b) SF1670 treated, (c) Wortmannin treated, and (d) Y27632 treated. Data represent the mean of at least three independent determinations; errors represent the standard error in the mean.

packing density compared with untreated, resulting in a lower compacted aggregate.[31]

Aggregation-induced PI3K modulation of the mitochondria showed significant downregulation when aggregates were treated with SF1670 for all sizes, and a significant increase with Wortmannin for all sizes (Table 1). Reduced compaction after treatment with Y27632 also resulted in significantly increased mitochondrial activity for all sizes. Analyzing glycolytic ATP also showed significant increases for 10k, 30k, and 50k when treated with SF1670, and treatment with Wortmannin resulted in a significant decrease for all sizes. Similarly, treatment with Y2632 also resulted in a significant reduction in glycolytic ATP for all sizes (Table 1).

Breaking this down into glucose and lactate showed that treatment with SF1670 resulted in a significant increase in glucose consumption for all sizes, and treatment with Wortmannin resulted in a significant decrease for all sizes (Table 2). Lactate showed a significant increase for all sizes as well when treated with SF1670, and all sizes showed a significant decrease when treated with Wortmannin. Relaxing the cytoskeleton with Y27632 treatment leads to a significant decrease in glucose consumption and lactate production as well (Table 2).

Size-dependent cortical stress results in mitochondrial fragmentation in 3D aggregates

To investigate the mitochondrial fission/fusion state and morphology, hASC aggregates of different sizes were dissociated and re-plated on adherent plates. The mitochondria were stained with MitoTracker Red CMXRos and imaged on a fluorescent microscope (Fig. 5A). The aspect ratio, the ratio of major to minor axes, of the mitochondrion was used to show that aggregation significantly reduces the mitochondrial fused state. The planar aspect ratio is 1.82 ± 1.08, whereas the aggregates range from 1.40 ± 0.41 to 1.59 ± 0.62 in the 10k and 50k; however, the aggregates did not show a significant difference from each other (Fig. 5B). Circularity, the ratio between the area and the perimeter, was significantly increased between the planar and 10k spheroids with 0.699 ± 0.27 and 0.814 ± 0.22, respectively; however, the planar was not statistically different than the 30k (0.748 ± 0.278) or 50k (0.685 ± 0.287) (Fig. 5C). Analysis by qPCR for fission proteins responsible for splitting the mitochondria showed a significant inverse size dependence for mitochondrial fission 1 protein (FIS1) and dynamin-1-like protein (*Drp1*). Fusion genes mitofusin-1 (*MFN1*) and mitofusin-2 (*MFN2*) showed significantly higher levels for 10 and 30k, whereas 50k was reduced (Fig. 5D).

Release of AldoA plays a key role in aggregation-induced metabolic reprogramming

Aggregation-induced AldoA enzyme activity was measured via a modified Jagannathan/Boyer hydrazine conversation assay.[23] Total and soluble AldoA enzyme was collected from cell lysate and from permeabilized aggregate cells. Total AldoA was significantly increased in aggregates of all sizes compared with planar (Fig. 6A, C, and D), with planar having a conversation rate of $5 \times 10^{-8} \pm 0.6$ (relative absorbance), and 10k and 50k having $5.2 \times 10^{-7} \pm 0.4$ and $9.8 \times 10^{-8} \pm 0.2$, respectively (Fig. 6a). Total AldoA can be either soluble or immobile and the ratio within the 10k aggregate showed a 2.1 ± 0.1-fold increase, whereas the 50k showed a 1.5 ± 0.1-fold increase over planar (Fig. 6B). The genes controlling AldoA were analyzed by qPCR, which showed an inverse size-dependent relationship for *AldoA*; the same was observed for *Akt1*, whereas PI3K showed no significant change (Fig. 6C). Western blot analysis of AldoA showed increased protein concentration for all sizes over planar, and an increased level of p-Akt in an inverse size-dependent fashion. Both p-PI3K and p-Abl1 showed higher activity in the aggregates than in planar, and they were significantly higher in the 10k. To test the mechanical pathway upregulation of PI3K hypothesized herein, Western blots of cells treated with either Y27632 or Gleevec, an Abl1 inhibitor, were carried out. We observed a significant loss of p-PI3 K upregulation in the 10k after treatment (Supplementary Fig. S3).

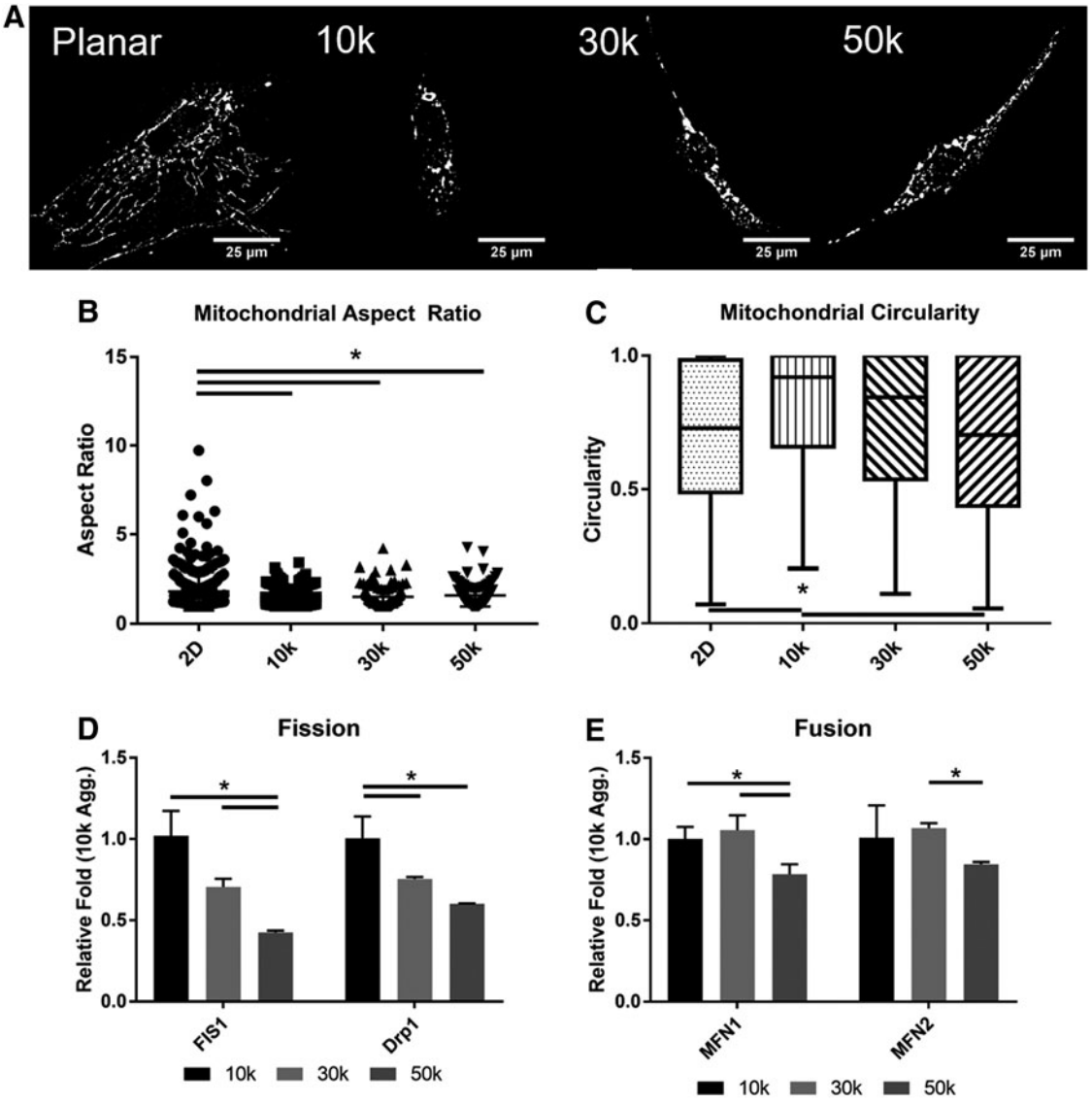

FIG. 5. Images of ASC size-controlled mitochondrial fission and fusion. **(A)** Planar and dissociated aggregate cells were stained with Mitotracker to highlight the shape of the mitochondria (scale bars are 25 μm). **(B)** Mitochondrial elliptical aspect ratio was calculated by dividing the major axis by the minor axis. **(C)** Mitochondrial circularity was calculated by dividing the area by the perimeter squared. **(D)** qPCR results for mitochondrial fusion genes. **(E)** PCR results for mitochondrial fission genes. Data represent the mean of at least three independent determinations; errors represent the standard error in the mean. $*p < 0.05$. PCR, polymerase chain reaction.

Discussion

Limited oxygen consumption and shift to glycolysis suggests a mechanical component

It has long been held that aggregates form hypoxic cores, and that they are responsible for altering cellular function. However, noninvasive evaluation of oxygen tension by Rudpp showed only a slight reduction of ~11% in the oxygen tension for our largest size (50k) (Fig. 1B); suggesting that metabolic reprogramming in hASC aggregates takes place in lieu of oxygen depletion. Murphy *et al.* also evaluated oxygen tension in MSC aggregates of differing sizes and concluded that oxygen tension varied similarly by less than 10% between the core and edge in 60k aggregates.[10] They also observed a size dependence in OCR similar to the trend shown in Figure 1C, but they attributed this to size-induced changes in diffusivity.[10] Our compaction results suggest biomechanical-associated metabolic reprogramming as the major mechanism due to the small change in oxygen tension and lack of sufficient diffusion barrier. Using the same method as that for aggregates, the OCR for planar culture was determined to be 99.9 fmol/cell/h, which is comparable to the OCR of 98.9 fmol/cell/h for planar bone marrow-derived MSCs reported by Curcio *et al.*[26] and Pattappa *et al.*[32] We consider planar culture to be the unprogrammed state, and there is a very clear trend of increasing OCR with increasing size, suggesting a reduction in the level of reprogramming, which illustrates a connection between aggregate diameter and the extent of compaction and metabolic reprogramming.

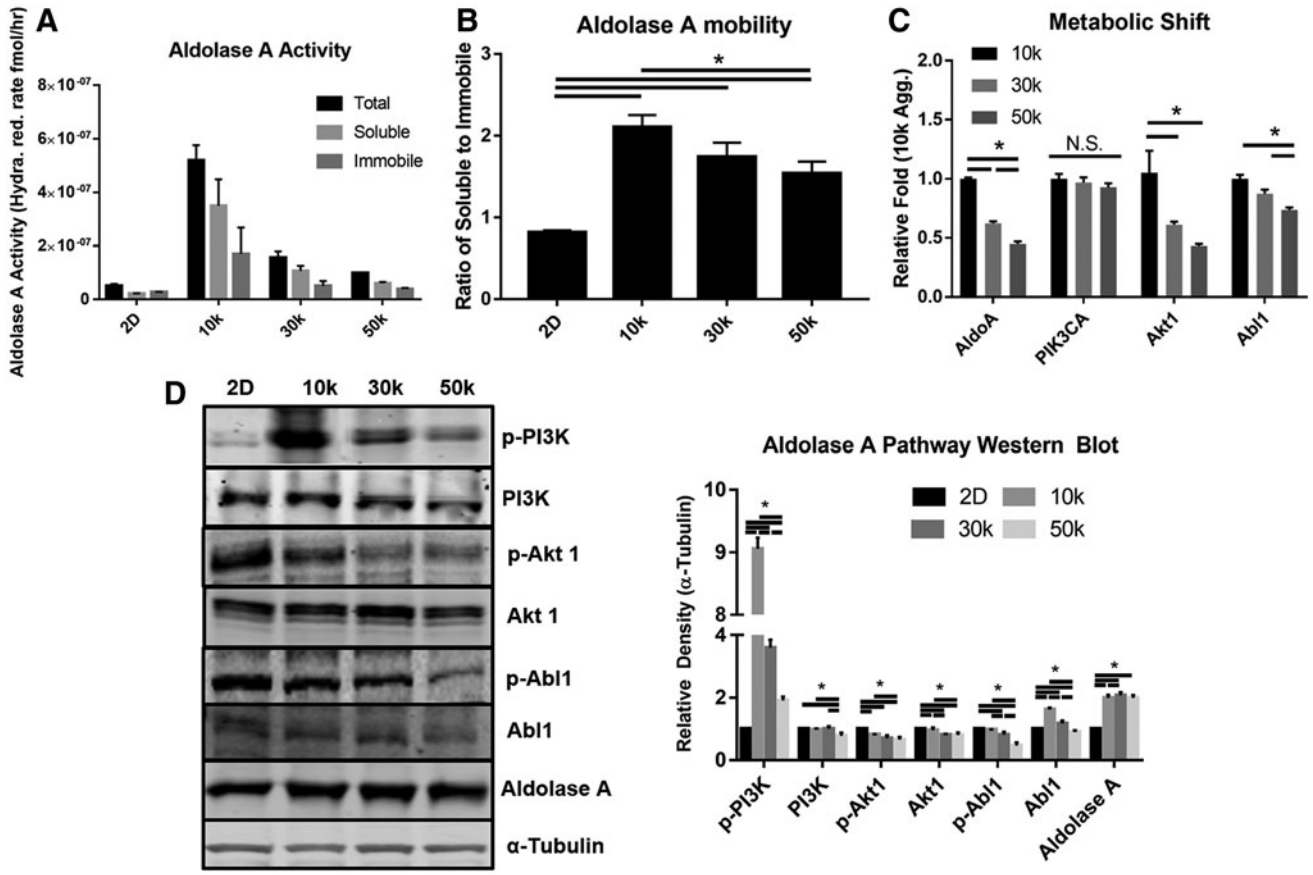

FIG. 6. AldoA hydrazine reduction assay results. **(A)** Size-dependent availability of AldoA. **(B)** Ratio of soluble to immobile AldoA for size-controlled aggregates. **(C)** qPCR for selected Aldolase response targets. **(D)** Western blot results for selected Aldolase and PI3K targets. Data represent the mean of at least three independent determinations; errors represent the standard error in the mean. AldoA, Aldolase A.

Strengthening this, glycolytic activity was observed to be size dependent, with the 10k aggregate utilizing more glucose and producing more lactate than the other sizes (Fig. 2A, B). A biomechanical gradient resulting from zonal aggregate structure was postulated as the driving force for this reprogramming. When contraction was withdrawn, by the administration of Y27632, a reduction of the glycolytic state and increased mitochondrial activity was observed (Tables 1 and 2). This is further strengthened by the size-dependent expression of glycolytic genes such as *G6PD* and *PKM2*, mitochondrial pyruvate gene *PDHA1*, and mitochondrial activities (Fig. 2F). Together, these results support a model where metabolic reprogramming is a result of size-dependent mechanical compaction rather than oxygen tension.

Mitochondrial dynamics can further explain the observed glycolytic trends as the balance between mitochondrial fusion and fission is essential to regulating cellular stress; fusion mitigates mitochondrial defects, and fission aids in ATP production in times of high metabolic demand.[33] Utilizing MitoTracker staining, differences in the mitochondrial condition became apparent. Planar ASC mitochondrion showed a highly connected network (Fig. 5A), whereas aggregate-derived cells exhibited hyper-fragmentation (Fig. 4B). Literature has shown that hyper-fragmentation results in mitochondrial dysfunction,[33] which correlates well with observed OCR (Fig. 1C) and mitochondrial function in aggregated cells (Fig. 2E). Recent literature has also shown that an influx of Ca^{2+}, similar to that observed in the cortical edge (Fig. 3Aii), leads to increased calmodulin kinase II activity in neural cells, which can increase mitochondrial fission by phosphorylating Drp1, a mitochondrial membrane protein responsible for cinching and cleaving the mitochondrion.[34,35] Indeed, *Drp1* gene expression is size dependent, with the highest expression in the 10k aggregate (Fig. 5D). Influxes of Ca^{2+} have also been shown in cancer to activate specific tyrosine kinases that can inhibit pyruvate kinases from allowing pyruvate to enter the TCA cycle,[36] which closely resembles our mitochondrial and glycolytic findings for cortical compaction. These results show that aggregation changes mitochondrion dynamics and leads to a more rounded and fragmented mitochondrion state that corresponds with lower oxidative respiration in a size-dependent manner.

Size-dependent aggregation induces a heterogeneous biomechanical cellular niche

Cell–cell and cell–ECM adhesions are major interactions that support 3D cellular organization and are vital to modulating stem cell fate and properties. Recent literature on cell–cell adhesions via cadherins has shown that they

stabilize actin *in situ* by disabling the conversion of fibrous actin to globular actin,[37–40] leading to increased actomyosin contraction. We observed just such E-cadherin and F-actin localization in the cortical region of all sizes but dissipating with size (Fig. 3Ai,ii and D),[37,38] which Murphy *et al.*[10] also observed. Similar F-actin contractile rings have been observed by Närvä *et al.* while analyzing hiPSC colonies. As hiPSC colonies develop, they construct a cortical ''actin fence'' comprising what appeared to be ventral stress fibers (VSFs), which contract, resulting in a biomechanical gradient. Interestingly, as the diameter of the colony increased, the VSFs became more linearly aligned, resulting in wider inter-fiber angles, a reduction in mechanical stress on individual cells at the edge, and a reduction in stemness.[41] This phenomenon closely resembles the observed mechanical stress reduction found as the aggregates increase in diameter. Cell–ECM interactions, through integrin-FAK complexes, also play an important role in regulating biomechanical signals that can alter stem cell fate.[42] Immunohistochemical assessment showed a decline in E-cadherin distribution with increasing size, whereas histologic assessment showed increasing levels of ECM deposition (Fig. 3). Taken together, these findings suggest a switch from cell–cell adhesions to cell–ECM adhesions as aggregate size increases.

Analysis of protein levels corroborated the size-dependent switch from cell–cell to majority cell–ECM trends showing increased collagen I, fibronectin, and p-FAK, a sign of focal adhesion activity and ECM stress induction (Fig. 4) with increasing diameter. Similarly, total protein/DNA showed an increasing trend with size (Supplementary Fig. S2), which we attributed to ECM protein deposition. On the other side, the 10k aggregate showed increased protein expression of p-catenin, p-vinculin Y822, and E-cadherin, all of which are cell–cell interaction/stress related. This strengthens the cell–cell rather than cell–ECM connection as recent literature on cellular mechanotransduction has shown that mechanical pulling by E-cadherin adhesions activates Abelson murine leukemia 1 (Abl1), a nonreceptor tyrosine kinase, responsible for the subsequent phosphorylation of vinculin.[37,28] Similarly, protein expression for both Abl1 and p-Abl1 was higher in the 10k aggregate (Fig. 6D).

Biomechanical gradient-induced PI3K pathway is responsible for signaling metabolic shift and inhibiting mitochondrial activity

Biomechanical stress has been shown to activate PI3K in multiple cell types from differentiated cells such as fibroblasts[43] and epithelial cells[44,45] to embryonic stem cells[46] and hMSCs.[47,37] PI3K-driven cytoskeletal reorganization, similar to that observed in VSF formation (Fig. 3Ai), can then feed-forward activate further PI3K.[48] It is our hypothesis that cell–cell-induced mechanical signaling induces Abl1 to phosphorylate PI3K, bridging the connection between mechanical and chemical signaling. This was supported by Western blot analysis of Gleevec and Y27632-treated cells, which showed a near-complete loss of p-PI3K in the 10k aggregate (Supplementary Fig. S3). PI3K signaling was modulated by using SF1670 and Wortmannin. SF1670 resulted in a mean lower OCR, lower mitochondrial activity (Table 1), and an increase in the glucose and lactate rates (Table 2). Conversely, treatment with Wortmannin resulted in an increase in OCR and greater mitochondrial activity in the aggregates, resulting in a reduction of glycolytic reprogramming (Table 1). Taken together, these results show the importance of PI3K activity in maintaining and altering metabolic reprogramming and show a connection between size/mechanical stress and PI3K activity. Hu *et al.* similarly blocked PI3K and examined the metabolism and mitochondrial activity of human mammary epithelial cells. They observed a decrease in the extracellular acidification rate and ratio of $NADH/NAD^+$ in response to blocking with BKM120 and BYL719, general PI3K and PI3Kα inhibitor, respectively,[44] which is mirrored in the blocking results found herein (Table 1). Prior studies have shown that PI3K/Akt signaling increases glucose transporter expression, enhances glucose uptake and phosphofructokinase activity,[48] similar to the metabolic reprogramming observed herein in the aggregates. Together, these results illustrate the importance of PI3K in metabolic reprogramming and show that PI3K is activated in the aggregate in a size-dependent fashion.

AldoA plays a key role in transducing mechanical signals to metabolic reprogramming

AldoA converts Fruc-1,6-BP to glyceraldehyde 3-phosphate and dihydroxyacetone phosphate in the glycolysis pathway and has been shown to be capable of shifting the metabolism of a cell from oxidative phosphorylation to glycolysis[44]; however, AldoA is *in vivo* sequestered on F-actin but is released in response to external stimulation.[44,49–51] The results herein have shown that aggregation induces a higher level of AldoA than planar culture, along with a size-dependent increase in the soluble to immobile ratio correlating stress and release (Fig. 6A, B). Previous literature has shown a connection between PI3 K and the release of AldoA.[44] We observed an increase in p-PI3K by Western blot in the 10k aggregate, which we suspect aids in the release of AldoA (Fig. 6D). When aggregates were treated with SF1670, we observed increased solubility of AldoA across the board. Treatment with Wortmannin, however, reduced soluble AldoA for all conditions (Supplementary Fig. S3). This is corroborated by Hu *et al.*, who likewise found that when mammary epithelial cells were treated with a PI3 K inhibitor AldoA solubility/activity similarly decreased. Herein, we have shown that smaller aggregates have higher levels of PI3K activity (Tables 1 and 2; Fig. 6D) and mechanical stress (Fig. 2).

Conclusion

Reported herein are several important findings pertaining to cortical compaction and the mechanism underpinning metabolic reconfiguration and functional activation in hASC aggregates. As diameter is the most important design parameter in creating spherical aggregates, this study delineates how it contributes to metabolic reprograming. We verified limited reduction in oxygen tension in 3D aggregates and then showed that mechanical stress due to cortical compaction rather than oxygen depletion plays a key role in metabolic reconfiguration. The results further demonstrate that mechanically activated PI3K and the release of AldoA explain how hMSC aggregation elevates hypoxic response genes and proteins, and increased phosphorylation of Akt, in lieu of a substantial biomolecular gradient.

Acknowledgments

The authors would like to thank Dr. Brian Washburn and Ms. Kristina Poduch of FSU Department of Biomedical Sciences for performing qRT-PCR experiments. This work was supported by the National Science Foundation (CBET #1743426) and NIH (R01NS102395-01A1).

Disclosure Statement

No competing financial interests exist.

Supplementary Material

Supplementary Data
Supplementary Figure S1
Supplementary Figure S2
Supplementary Figure S3

References

1. Song, W.J., Li, Q., Ryu, M.O., *et al.* TSG-6 Secreted by human adipose tissue-derived MEsenchymal stem cells ameliorates DSS-induced colitis by inducing M2 macrophage polarization in mice. Sci Rep **7,** 5187, 2017.
2. Espagnolle, N., Balguerie, A., Arnaud, E., Sensebé, L., and Varin, A. CD54-mediated interaction with pro-inflammatory macrophages increases the immunosuppressive function of human mesenchymal stromal cells. Stem Cell Rep **8,** 961, 2017.
3. Bhang, S.H., Cho, S.W., La, W.G., *et al.* Angiogenesis in ischemic tissue produced by spheroid grafting of human adipose-derived stromal cells. Biomaterials **32,** 2734, 2011.
4. Fennema, E.M., Tchang, L.A.H., Yuan, H., *et al.* Ectopic bone formation by aggregated mesenchymal stem cells from bone marrow and adipose tissue: a comparative study. J Tissue Eng Regen Med **12,** e150, 2018.
5. Dang, P.N., Dwivedi, N., P.L.M., *et al*. sberg, Controlled dual growth factor delivery from micoparticles incorporated within human bone marrow-derived mesenchymal stem cell aggregates for enhanced bone tissue engineering via endochondral ossification. Stem Cells Transl Med **5,** 2016.
6. Cho, R.J., Kim, Y.S., Kim, J.Y., and Oh, Y.M. Human adipose-derived mesenchymal stem cell spheroids improve recovery in a mouse model of elastase-induced emphysema. BMB Rep **50,** 79, 2017.
7. Takebe, T., Enomura, M., Yoshizawa, E., *et al.* Vascularized and complex organ buds from diverse tissues via mesenchymal cell-driven condensation. Cell Stem Cell **16,** 556, 2015.
8. Kasinskas, R.W., Venkatasubramanian, R., and Forbes, N.S. Rapid uptake of glucose and lactate, and not hypoxia, induces apoptosis in three-dimensional tumor tissue culture. Integr Biol **6,** 399, 2014.
9. van Winkle, A.P., Gates, I.D., and Kallos, M.S. Mass transfer limitations in embryoid bodies during human embryonic stem cell differentiation. Cells Tissues Organs **196,** 34, 2012.
10. Murphy, K.C., Hung, B.P., Browne-Bourne, S., *et al.* Measurement of oxygen tension within mesenchymal stem cell spheroids. J R Soc Interface **14,** 2017.
11. Costa, M.H.G., McDevitt, T.C., Cabral, J.M.S., da Silva, C.L., and Ferreira, F.C. Tridimensional configurations of human mesenchymal stem/stromal cells to enhance cell paracrine potential towards wound healing processes. J Biotechnol **262,** 28, 2017.
12. Wobma, H.M., Liu, D., and Vunjak-Novakovic, G. Paracrine effects of mesenchymal stromal cells cultured in three-dimensional settings on tissue repair. ACS Biomater Sci Eng **4,** 1162, 2018.
13. Cesarz, Z., Funnell, J.L., Guan, J., and Tamama, K. Soft elasticity-associated signaling and bone morphogenic protein 2 are key regulators of mesenchymal stem cell spheroidal aggregates. Stem Cells Dev **25,** 622, 2016.
14. Ingber, D.E. Tensegrity-based mechanosensing from macro to micro. Prog Biophys Mol Biol **97,** 163, 2008.
15. Frith, J.E., Thomson, B., and Genever, P.G. Dyanamic three-dimensional culture methods enhance mesenchymal stem cell properties and increase therapeutic potential. Tissue Eng C Methods **16,** 735, 2009.
16. Cheng, N.-C., Wang, S., and Young, T.-H. The influence of spheroid formation of human adipose-derived stem cells on chitosan films on stemness and differentiation capabilities. Biomaterials **33,** 1748, 2012.
17. Kretlow, J.D., Jin, Y.Q., Liu, W., *et al.* Donor age and cell passage affects differentiation potential of murine bone marrow-derived stem cells. BMC Cell Biol **9,** 60, 2008.
18. Scruggs, B.A., Semon, J.A., Zhang, X., *et al.* Age of the donor reduces the ability of human adipose-derived stem cells to alleviate symptoms in the experimental autoimmune encephalomyelitis mouse model. Stem Cells Transl Med **2,** 797, 2013.
19. Choi, Y.S., Vincent, L.G., Lee, A.R., Dobke, M.K., and Engler, A.J. Mechanical derivation of functional myotubes from adipose-derived stem cells. Biomaterials **33,** 2482, 2012.
20. Kim, J., and Ma, T. Bioreactor strategy in bone tissue engineering: pre-culture and osteogenic differentiation under two flow configurations. Tissue Eng A **18,** 2354, 2012.
21. Guarino, R.D., Dike, L.E., Haq, T.A., Rowley, J.A., Pitner, J.B., and Timmins, M.R. Method for determining oxygen consumption rates of static cultures from microplate measurements of pericellular dissolved oxygen concentration. Biotechnol Bioeng **86,** 775, 2004.
22. Liu, Y., Muñoz, N., Tsai, A.C., Logan, T.M., and Ma, T. Metabolic reconfiguration supports reacquisition of primitive phenotype in human mesenchymal stem cell aggregates. Stem Cells **35,** 398, 2017.
23. Jagannathan, V., Singh, K., and Damodaran, M. Carbohydrate metabolism in citric acid fermentation. 4. Purification and properties of aldolase from *Aspergillus niger*. Biochem J **63,** 94, 1956.
24. Engler, A.J., Sen, S., Sweeney, H.L., and Discher, D.E. Matrix elasticity directs stem cell lineage specification. Cell **126,** 677, 2006.
25. Kilian, K.A., Bugarija, B., Lahn, B.T., and Mrksich, M. Geometric cues for directing the differentiation of mesenchyal stem cells. *PNOS* **107,** 4872, 2010.
26. Curcio, E., Piscioneri, A., Morelli, S., Salerno, S., Macchiarini, P., and de Bartolo, L.. Kinetics of oxygen uptake by cells potentially used in a tissue engineered trachea. Biomaterials **35,** 6829, 2014.
27. Turlier, H., and Maitre, J.-L. Mechanics of tissue compaction. Semin Cell Dev Biol **47–48,** 110, 2015.
28. Bays, J.L., Peng, X., Tolbert, C.E., *et al.* Vinculin phosphorylation differentially regulates mechanotransduction at cell-cell and cell-matrix adhesions. J Cell Biol **205,** 251, 2014.

29. Carnero, A., Blanco-Aparicio, C., Renner, O., Link, W., and Leal, J.F. The PTEN/PI3K/akt signalling pathway in cancer, therapeutic implications. Curr Cancer Drug Targets **8,** 187, 2008.
30. Walker, E.H., Pacold, M.E., Perisic, O., *et al.* Structural determinants of phosphoinositide 3-kinase inhibition by wortmannin, LY294002, quercetin, myricetin, and staurosporine. Mol Cell **6,** 909, 2000.
31. Tsai, A.C., Liu, Y., Yuan, X., and Ma, T. Compaction, fusion, and functional activation of three-dimensional human mesenchymal stem cell aggregate. Tissue Eng A **21,** 1705, 2015.
32. Pattappa, G., Heywood, H.K., de Bruijn, J.D., and Lee, D.A. The metabolism of human mesenchymal stem cells during proliferation and differentiation. J Cell Physiol **226,** 2562, 2011.
33. Rambold, A.S., and Pearce, E.L. Mitochondrial dynamics at the interface of immune cell metabolism and function. Trends Immunol **39,** 6, 2018.
34. Han, X.J., Lu, Y.F., Li, S.A., *et al.* CaM kinase Ialpha-induced phosphorylation of Drp1 regulates mitochondrial morphology. J Cell Biol **182,** 573, 2008.
35. Patergnani, S., Suski, J.M., Agnoletto, C., *et al.* Calcim signaling around the mitochondria associated membranes (MAMs). Cell Commun Signal **9,** 19, 2011.
36. Martini, M., De Santis, M.C., Braccini, L., Gulluni, F., and Hirsch, E. PI3K/AKT signaling pathway and cancer: an updated review. Ann Med **46,** 372, 2014.
37. Han, M.K.L., and de Rooij, J. Resolving the cadherin-F-actin connection. Nat Cell Biol **19,** 14, 2016.
38. Engl, W., Arasi, B., Yap, L., Thiery, J., and Viasnoff, V. Actin dynamics modulate mechanosensitive immobilization of E-cadherin at adherens junctions. Nat Cell Biol **16,** 584, 2014.
39. Han, M.K., and de Rooij, J. Converging and unique mechanisms of mechanotransduction at adhesion sites. Trends Cell Biol **26,** 612, 2016.
40. Bertocchi, C., Wang, Y., Ravasio, A., *et al*. Nanoscale architecture of cadherin-based cell adhesions.. Nat Cell Biol **19,** 28, 2017.
41. Närvä, E., Stubb, A., Guzmán, C., *et al.* A strong contractile actin fence and large adhesions direct human pluripotent colony morphology and adhesion. Stem Cell Rep **9,** 67, 2017.
42. Kim, I.G., Ko, J., Lee, H.R., Do, S.H., and Park, K. Mesenchymal cells condensation-inducible mesh scaffolds for cartilage tissue engineering. Biomaterials **85,** 18, 2016.
43. Katsumi, A., Naoe, T., Matsushita, T., Kaibuchi, K., and Schwartz, M.A. Integrin activation and matrix binding mediate cellular responses to mechanical stretch. J Biol Chem **280,** 16546, 2005.
44. Hu, H., Juvekar, A., Lyssiotis, C.A., *et al.* Phosphoinositide 3-kinase regulates glycolysis through mobilization of aldolase from the actin cytoskeleton. Cell **164,** 433, 2016.
45. Vasilyev, A., Liu, Y., Hellman, N., Pathak, N., and Drummond, I.A. Mechanical stretch and PI3K signaling link cell migration and proliferation to coordinate epithelial tubule morphogenesis in the zebrafish pronephros. PLoS One **7,** e39992, 2012.
46. Horiuchi, R., Akimoto, T., Hong, Z., and Ushida, T. Cyclic mechanical strain maintains Nanog expression through PI3K/Akt signaling in mouse embryonic stem cells. Exp Cell Res **318,** 1726, 2012.
47. Hao, J., Zhang, Y., Jing, D., *et al.* Mechanobiology of mesenchymal stem cells: perspective into mechanical induction of MSC fate. Acta Biomater **20,** 1, 2015.
48. Lien, E.C., Dibble, C.C., and Toker, A. PI3K signaling in cancer: beyond AKT. Curr Opin Cell Biol **45,** 62, 2017.
49. Mercurio, L., Cecchetti, S., Ricci, A., *et al.* Phosphatidylcholine-specific phospholipase C inhibition down- regulate CXCR4 expression and interferes with proliferation, invasion and glycolysis in glioma cells. PLoS One **12,** e0176108, 2017.
50. Dupuy, F., Tabariès, S., Andrzejewski, S., *et al.* PDK1-dependent metabolic reprogramming dictates metastatic potential in breast cancer. Cell Metab **22,** 577, 2015.
51. Faubert, B., Vincent, E.E., Griss, T., *et al.* Loss of the tumor suppressor LKB1 promotes metabolic reprogramming of cancer cells via HIF-1α. Proc Natl Acad Sci U S A **111,** 2554, 2014.

Address correspondence to:
Teng Ma, PhD
Department of Chemical and Biomedical Engineering
FAMU-FSU College of Engineering
Florida State University
2525 Pottsdamer Street
Tallahassee, FL 32310

E-mail: teng@eng.fsu.edu

Received: May 31, 2018
Accepted: August 31, 2018
Online Publication Date: April 11, 2019